This is the Pre-Published Version.

This is the peer reviewed version of the following article: H. Zhang, Z. Chen, M. Qin, Z. Ren, K. Liu, J. Huang, D. Shen, Z. Wu, Y. Zhang, J. Hao, C.-s. Lee, X. Lu, Z. Zheng, W. Yu, G. Li, Multifunctional Crosslinking-Enabled Strain-Regulating Crystallization for Stable, Efficient α-FAPbI3-Based Perovskite Solar Cells. Adv. Mater. 2021, 33, 2008487, which has been published in final form at https://doi.org/10.1002/adma.202008487. This article may be used for non-commercial purposes in accordance with Wiley Terms and Conditions for Use of Self-Archived Versions. This article may not be enhanced, enriched or otherwise transformed into a derivative work, without express permission from Wiley or by statutory rights under applicable legislation. Copyright notices must not be removed, obscured or modified. The article must be linked to Wiley's version of record on Wiley Online Library and any embedding, framing or otherwise making available the article or pages thereof by third parties from platforms, services and websites other than Wiley Online Library must be prohibited.

Multi-functional Cross-linking Enabled Strain Regulating Crystallization for Stable, Efficient α-$FAPbI_3$-based Perovskite Solar Cells

Hengkai Zhang[1,2], Zhiliang Chen[1], Minchao Qin[3], Zhiwei Ren[1,2], Kuan Liu[1,2], Jiaming Huang[1,2], Dong Shen[4], Zehan Wu[5], Yaokang Zhang[6], Jianhua Hao[5], Chun-sing Lee[4], Xinhui Lu[3], Zijian Zheng[6], Wei Yu[1,7], Gang Li[1,2*]*

Affiliations:

[1]Department of Electronic and Information Engineering, Research Institute for Smart Energy (RISE), The Hong Kong Polytechnic University, Hung Hom, Kowloon, Hong Kong, China

[2]The Hong Kong Polytechnic University Shenzhen Research Institute, Shenzhen 518057, China

[3]Department of Physics, The Chinese University of Hong Kong, New Territories, Hong Kong, China

[4]Center of Super-Diamond and Advanced Films (COSDAF) and Department of Chemistry, City University of Hong Kong, Kowloon, Hong Kong, China

[5]Department of Applied Physics, The Hong Kong Polytechnic University, New Territories, Hong Kong, China

[6]Laboratory for Advanced Interfacial Materials and Devices, Research Centre for Smart Wearable Technology, Institute of Textiles and Clothing, The Hong Kong Polytechnic University, Hung Hom, Kowloon, Hong Kong, China

[7]State Key Laboratory of Catalysis, Dalian Institute of Chemical Physics, Chinese Academy of Sciences, Dalian National Laboratory for Clean Energy, Dalian 116023, Liaoning, China

* Correspondence author. Email: wyu@dicp.ac.cn (W.Y.); gang.w.li@polyu.edu.hk (G.L.)

Keywords: perovskite solar cell, α-$FAPbI_3$, strain regulation, cross-linking, defects passivation

Abstract

α-$FAPbI_3$ represents the state-of-the-art in perovskite solar cells but experiences intrinsic thermal-induced tensile strain due to a higher phase converting temperature, which is one critical instability factor. An *in situ* Cross-linking enabled Strain Regulating Crystallization (CSRC) method with trimethylolpropane triacrylate (TMTA) is introduced to precisely regulate the top section of perovskite film where the largest lattice distortion occurs. In CSRC, cross-linking provides *in situ* perovskite thermal expansion confinement and strain regulation during the annealing crystallization process, which is proven to be much more effective than the conventional strain compensation (post-treatment) method. Moreover, the CSRC with TMTA successfully achieves multi-functionality simultaneously: the regulation of tensile strain, perovskite defects passivation with an enhanced V_{OC} (50 mV), and enlarged perovskite grain size. The CSRC approach gives significantly enhanced PCE of 22.39% in α-$FAPbI_3$-based PSC vs. 20.29% in the control case. More importantly, the control PSCs' instability factor – residual tensile strain is regulated into compression strain in the CSRC perovskite film through TMTA cross-linking, resulting in not only the best PCE but also outstanding device stability in both long-term storage (over 4000 h with 95% of initial PCE) and light soaking (1248 h with 80% of initial PCE) conditions.

Introduction

Organic-inorganic metal halide perovskite solar cell (PSC), as one of the most promising research topics in material science, has attracted keen attention for its low-

cost, solution-processed fabrication, and excellent optoelectronic properties.[1-7] Great advancement has been achieved in the area of PSCs, where the power conversion efficiency (PCE) of PSCs has raised from 3.8%[8] to a certified 25.5% PCE in less than 13 years.[9] The formamidinium lead triiodide ($FAPbI_3$) with a narrower bandgap and thus greater light spectral response[10-16] has attracted wide interest and become the ideal light absorber material for PSCs. However, a higher annealing temperature is necessary for converting the δ-$FAPbI_3$ to α-$FAPbI_3$ (~150°C) compared with the $MAPbI_3$ case (~100 °C). Therefore the α-$FAPbI_3$ based perovskite experiences more severe stress (σ) due to the large temperature gradient: $\sigma_{\Delta T} = \frac{E_P}{1-\upsilon_p}(\alpha_s - \alpha_p)\Delta T$, where E_p is the modulus of the perovskite, υ_p is Poisson's ratio in the perovskite, α_s and α_p are the thermal expansion coefficients of the substrate and the perovskite film, respectively, and ΔT is the temperature difference of the annealing temperature of the perovskite film and room temperature[17]. When $\alpha_s < \alpha_p$, tensile strain is usually introduced in a perovskite film, and if $\alpha_s > \alpha_p$, the perovskite film bears compressive strain. Generally, tensile strain is bearing in the perovskite film. Here σ stands for tensile strain in the following description, unless otherwise noted.

The lattice tensile strain coming from the thermal expansion has recently been identified as a critical intrinsic instability factor for organic-inorganic hybrid perovskite,[18, 19] which significantly limits the stability of α-$FAPbI_3$-based high-efficiency PSCs. The perovskite film also exhibits inhomogeneous residual stress distribution across the film thickness direction – the top perovskite film region bears a more serious lattice tensile strain.[20] Recently, several methods have been introduced to

relax the lattice tensile strain towards enhancing the intrinsic stability of perovskite films,[10, 17-27] including the delicate modification of annealing process to regulate the thermal expansion,[21, 23] the residual tensile strain compensation through interface post-treatment[20, 25] and charge-transporting layers,[17] and composition alloying to modulate the strain by incorporating cesium (Cs)[10] and guanidinium (GA).[28] However, these methods are all associated with limitations. For example, the delicate modification annealing process requires precise control over the annealing temperature and annealing steps, which increases the fabrication difficulties; the previously reported strain compensation methods are post-treatment strategies, which can help to relax the strain of pre-formed perovskite film to certain extend only; for the composition alloying, the doping agent is fully dispersed in the precursor and it is difficult to precisely modulate the largest lattice distortion top region of the perovskite film.

Herein, a novel and effective strain engineering strategy – Cross-linking enabled Strain Regulating Crystallization (CSRC) – is introduced to precisely modulate the largest lattice distortion region through synchronous cooperation of *in situ* chemical cross-linking and perovskite crystallization. In this work, trimethylolpropane triacrylate (TMTA), with multiple functional groups of -OH and C=O (could provide effective passivation for the perovskite device [29, 30]), was selected as a chemical cross-linking agent, which will *in situ* cross-link into PTMTA (poly(trimethylolpropane triacrylate)) under moderate thermal treatment.[31, 32] TMTA is introduced into the anti-solvent chlorobenzene (CB), aiming at regulating the top region of the perovskite film during the crystallization process. The *in situ* chemical cross-linking strategy during the

perovskite crystallization process is proven to be much more effective in strain regulation over the conventional strain compensation method in which TMTA in isopropanol is applied as post-treatment. Additionally, the cross-linked device exhibits enlarged grain size, fewer defects, and reduced non-radiative recombination, leading to a remarkable V_{OC} enhancement (50 mV) and higher PCE of 22.39% compared with the control device of 20.29% PCE. The TMTA CSRC-treated PSCs also exhibited superior stability: 95% of the initial PCE after 4000 h long-term storage and the remaining 80% of the initial PCE after 1248 h light-illumination. The reported *in situ* CSRC approach exhibits multiple functions including strain regulation, humidity repulsion, effective trap passivation, and therefore highly efficient and stable PSCs are obtained simultaneously.

Results and discussion

The α-$FAPbI_3$-based perovskite films ($(FAPbI_3)_{0.95}(MAPbBr_3)_{0.05}$, with 10% excess of PbI_2 in precursor) were treated with TMTA via two different methods: conventional surface post-treatment and *in situ* CSRC method, as shown in **Figure 1**a. For the surface post-treatment, a perovskite film was first formed by the traditional CB antisolvent method followed by 150ºC annealing of 20 min; then TMTA dissolved into IPA was coated on top, followed by another 150ºC 10 min annealing process. In the CSRC-treatment, TMTA was incorporated into CB as the antisolvent, followed by the cross-linking assisted perovskite crystallization occurring during the annealing process (150ºC, 10 min). The moderate thermal condition of 150ºC allows *in situ* cross-linking polymerization due to the three alkenyl groups in TMTA (**Figure 1**a).[33]

As revealed by X-ray diffraction (XRD) and grazing-incidence wide-angle X-ray scattering (GIWAXS) results, $FAPbI_3$ perovskite films were well-formed in both cases. The XRD patterns (Figure 1b) show the (001), (111), and (002) crystal planes of $FAPbI_3$ locating at 13.95°, 24.45°, and 28°, respectively. Compared to the control film (CB only antisolvent without any further treatment), the TMTA post-treated film exhibits similar XRD patterns, while the TMTA CSRC-treated film shows both reduced PbI_2 (12.6°) and δ-phase $FAPbI_3$ (12°) peak intensity, indicating the TMTA CSRC method can effectively suppress the formation of δ-phase $FAPbI_3$ (non-perovskite phase). The GIWAXS (Figure 1c) presents clear scattering rings at q of 1 $Å^{-1}$ and 2 $Å^{-1}$, which were corresponding with (001) and (002) planes, respectively. The control and TMTA post-treated films exhibited a distinct PbI_2 phase at q=0.9 $Å^{-1}$, while little PbI_2 phase appears on TMTA CSRC-treated film, which is consistent with the XRD results (Figure 1b). With the TMTA concentration increasing, the CSRC-treated films exhibited a similar reduction of PbI_2 at q=0.9 $Å^{-1}$ (Figure S1).

The morphology of perovskite films investigated by top view scanning electron microscope (SEM, Figure 1d) shows the existence of small grains at the clear boundaries of large grains, with the grain size as large as 1.5 μm for the control perovskite film. A similar morphology is observed for the TMTA post-treated films except for the blurred crystal surface and unclear grain boundaries, which may be caused by the polymerized TMTA on the surface. With the increase of TMTA concentration in IPA, the perovskite film was obscured by a thicker layer of polymerized TMTA polymer (Figure S2). For the TMTA CSRC-treated film, the

perovskite grain size further grows to 2 μm with unclear boundaries and fewer small grains, indicating the TMTA molecule crosslinking during the perovskite thermal conversion process can significantly facilitate the perovskite growth by merging small grains into large grains. This grain-grown phenomenon has similarities with the so-called "inter-grain crosslinking of the perovskite",[34] but it is through *in situ* crosslinking of molecules. The excess PbI_2 nanoparticles are obviously randomly distributed on the perovskite control films, while with the treatment of TMTA, either by post-treatment or CSRC-treatment, the flaky substances formed, which might benefit from the interaction between TMTA and PbI_2 crystal facets or/and from the cross-linking process enabling exposing of particular crystal facet[33, 35]. The flaky substance can be seen on the TMTA-PbI_2 sample (Figure S3), demonstrating it is due to the "interaction" of TMTA and PbI_2. As Luo et al. reported, the regulated distribution of excess PbI_2 may have a positive impact on the photophysical properties of the perovskite film[35]. From the cross-sectional SEM images, control film and TMTA treated films by CSRC and post-treatment all exhibited good crystallinity with smooth perovskite grain (Figure S4).

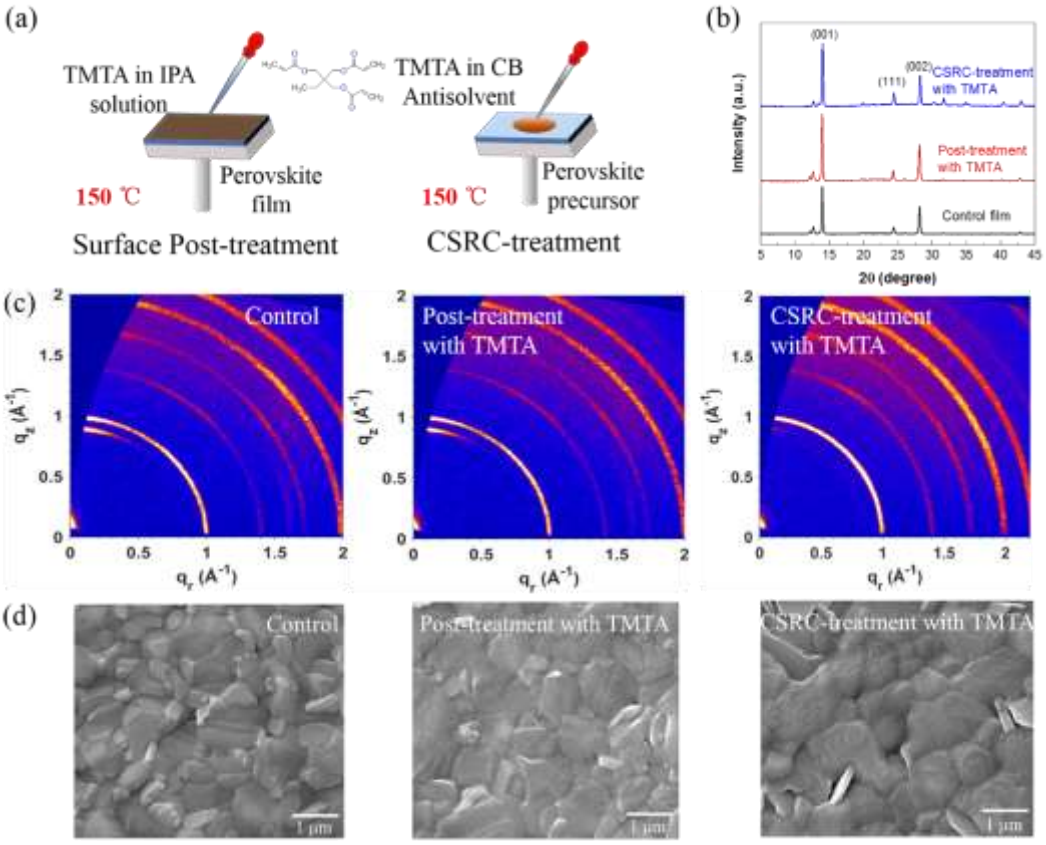

Figure 1. (a) Comparison of two different TMTA treatments of perovskite in this work: surface post-treatment and CSRC-treatment; (b) XRD patterns, (c) GIWAXS, and (d) SEM images of control, TMTA post-treated, and TMTA CSRC-treated perovskite films.

The conventional PSCs were adopted in this work with a device configuration of Glass/ITO/SnO_2/$(FAPbI_3)_{0.95}(MAPbBr_3)_{0.05}$/Spiro-OMeTAD/Au. The detailed experimental information was shown in the experimental section. The TMTA post-treatment and CSRC approaches were optimized by varying TMTA concentrations in IPA and CB, respectively (Figure S5 and Table S1). The *J-V* results (**Figure 2**a and **Table 1**) display that the best CSRC device with 0.1% TMTA yielded a PCE of 22.39% with a short circuit current (J_{SC}) of 24.8 mA cm^{-2}, open-circuit voltage (V_{OC}) of 1.15 V, and FF of 78.5%, higher than the optimized TMTA post-treated devices (0.3% in IPA,

PCE of 21.66%, J_{SC} of 24.8 mA cm^{-2}, V_{OC} of 1.14 V, and FF of 76.6%). Both of TMTA treated devices afford higher performance than the control PSC with PCE of 20.29%, J_{SC} of 24.5 mA cm^{-2}, V_{OC} of 1.10 V, and FF of 75.3%. The histogram of three types of devices (Figure 2b) and the statistic distribution of the photovoltaic parameters (Figure S6) exhibit the device reproducibility and further verify the PCE enhancement. The average values of J_{SC} for all three cases are almost identical. The enhanced V_{OC} and FF of TMTA post-treated (average of 1.12 V and 76.0%) and CSRC PSCs (average of 1.13 V and 76.0%) than the control one (average of 1.10 V and 74.5%) result in the improved average PCE of TMTA treated cells (post-treated of 20.3%, CSRC-treated of 20.7%, vs. the control of 19.6%). The forward-scan and reverse-scan results indicate a negligible hysteresis for the devices with TMTA CSRC-treatment (hysteresis index: 0.009) (Table S2). The external quantum efficiency (EQE, Figure 2c) spectra give the integrated J_{SC} values of 23.8, 23.5, and 23.9 mA cm^{-2} for the control, TMTA post-treated, and TMTA CSRC PSCs, respectively, which are in good agreement with the *J-V* results (within 5% deviation). There is a very slight blue-shift EQE onset (consistent with the UV-vis absorption onset shift in Figure S7) for the CSRC-treated device, indicating a slight enlarged bandgap. The steady-state power output (SPO) measurements in 500 s (Figure 2d) present a stable SPO PCE of 19.5%, 20.5%, and 21.4% for the control, TMTA post-treated, and TMTA CSRC devices, respectively. In order to demonstrate the universality of the proposed CSRC method, $FA_{0.93}MA_{0.04}Cs_{0.03}$-based PSC was prepared with CSRC approach, affording a PCE of 22.8% and up to 23.5% with anti-reflective film (Figure S8).

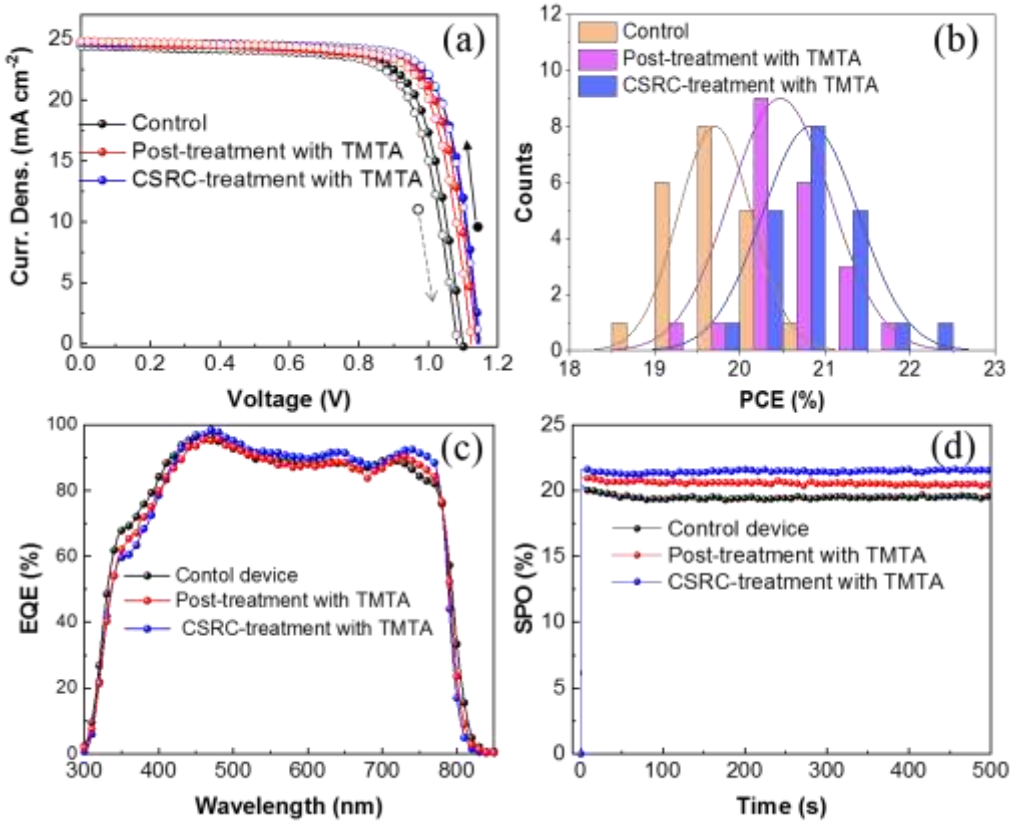

Figure 2. (a) Forward and reverse scan of the control, TMTA post-treated, and TMTA CSRC-treated PSCs. (b) Statistics of PCEs reference control, TMTA post-treatment, and TMTA CSRC devices. (c) External quantum efficiency (EQE), and (d) the steady-state power output of the corresponding PSCs.

Table 1. Optimized device parameters from the *J-V* measurements of the control, TMTA post-treated, and CSRC-treated PSCs.

Device	V_{OC} (V)	J_{SC} (mA cm^{-2})	$J_{SC\text{-}EQE}$ (mA cm^{-2})	FF (%)	PCE (%)
Control	1.10	24.5	23.8	75.3	20.29
TMTA post-treatment	1.14	24.8	23.5	76.6	21.66
TMTA CSRC-treatment	1.15	24.8	23.9	78.5	22.39

To elucidate the effect of TMTA, the trap density variation of the devices is

calculated by the space charge limited current (SCLC) method. The electron-only device with the structure of ITO/SnO_2/PSC/PCBM/Au (**Figure 3**a) is prepared and the dark *J-V* curves are shown in Figure 3b. The trap-filling limited voltage (V_{TFL}) is determined as the onset voltage of the trap-filling limited (TFL) region, and the corresponding trap density can be calculated using $V_{TFL} = \frac{q.n_{trap}L^2}{2\varepsilon_0\varepsilon}$, where q is the elementary charge, L is the thickness of the perovskite film (500 nm), ε_0 is the permittivity in vacuum (8.85×10^{12} F m^{-1}), and ε is the relative dielectric constant of $FAPbI_3$ (46.9). The electron trap densities n_{trap} of the control, TMTA post-treated, and TMTA CSRC devices are 2.13×10^{15}, 1.48×10^{15} and 1.42×10^{15} cm^{-3}, respectively. The lower trap density for TMTA-treated film indicates improved film quality and passivation effect.

Furthermore, the dependence of V_{OC} and J_{SC} on the light intensity from 10 to 100 mW cm^{-2} are examined. The V_{OC} *vs.* light intensity (Figure 3c) curves demonstrate that the V_{OC} is proportional to the logarithm of light intensity and the slopes are calculated to be 1.79 k_BT/q, 1.45 k_BT/q, and 1.23 k_BT/q for the control, TMTA post-treated, and TMTA CSRC PSCs, respectively, where k_B is the Boltzmann constant, T is the absolute temperature in Kelvin and q is the elementary charge. The decreased slope from the control device to TMTA treated devices means that the trap-assisted recombination is effectively suppressed by TMTA, resulting in the V_{OC} enhancement. The J_{SC} versus light intensity curves on a double-logarithmic scale (Figure 3d) can be fitted according to the relation of $J_{SC} \propto \Phi^{\alpha}$, where Φ corresponds to the light intensity and α to the exponent of the dependence. The calculated α values are 0.90, 0.98, and 0.99 for the control, post-

treated, and CSRC PSCs, respectively, suggesting the reduced bimolecular recombination with TMTA treatments.

The origin of enhanced TMTA-treated PSCs' performance is further uncovered by the steady-state photoluminescence (PL) and time-resolved photoluminescence (TRPL) spectra. As shown in Figure 3e, the TMTA post-treated and CSRC perovskite films present an eightfold and fifteenfold enhanced PL intensity than the control film, respectively, indicating the significantly reduced defect density in TMTA-treated perovskite films. The TRPL results (Figure 3f) exhibit that the PL decays much slower for the TMTA- treated films than the control. The spectra are fitted by the biexponential equation[36, 37]: $Y = A_1\exp(-t/\tau_1) + A_2\exp(-t/\tau_2)$, where τ_1 and τ_2 denote the fast and slow decay time constants, relating to the radiative and trap-assisted nonradiative recombination processes,[37] respectively (Table S3). The lifetime τ_2, on behave of trap-assisted nonradiative recombination, for the TMTA post-treated and CSRC films are calculated to be 1678.5 ns, and 2796.1 ns, respectively – both are much longer than that of control film (1004.9 ns), demonstrating lower defects density in TMTA treated films. Altogether, the reduced electron trap density (SCLC), suppressed trap-assisted and bimolecular recombination (V_{OC} and J_{SC} dependence on light intensity tests) and lower nonradiative recombination process (PL and TRPL) for TMTA treated PSCs result in improved device performance. Furthermore, the TMTA CSRS device has a lower trap density and longer PL lifetime than the TMTA post-treated one, identifying the better device performance of TMTA CSRC treatment, with inter-grain cross-linking.

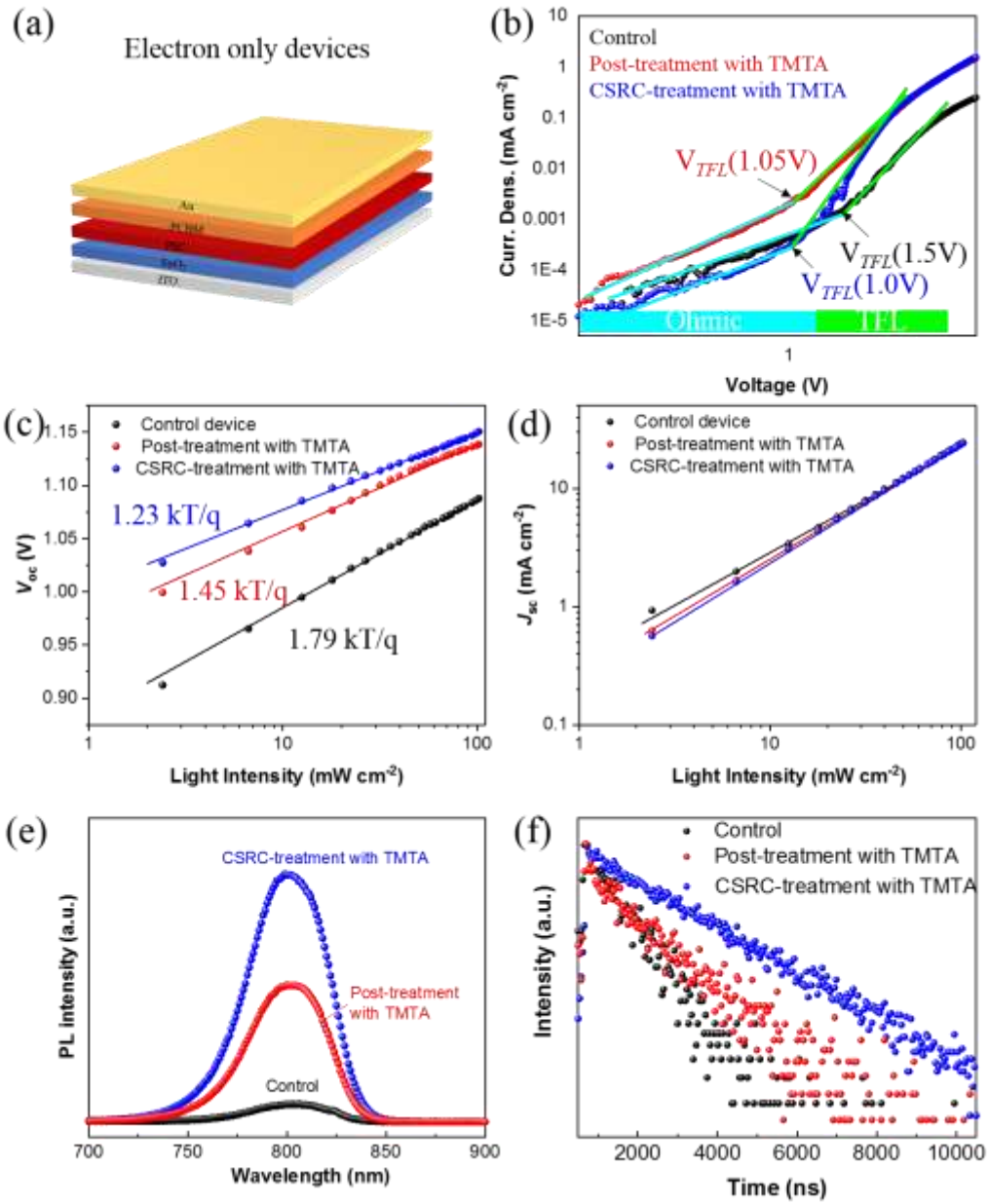

Figure 3. (a) Device structure of the electron-only device. (b) *J-V* curves of the SCLC measurements based on the electron-only device for the control and TMTA treated devices. (c) V_{OC} and (d) J_{SC} dependence on light intensity for the control and TMTA treated PSCs. (e) Steady-state PL and (f) TRPL analysis of perovskite films.

We then conducted X-ray photoelectron spectroscopy (XPS) depth profiling on the two optimized condition TMTA treated films (0.3% TMTA post-treatment and 0.1%

TMTA CSRC treatment). The Pb (**Figure 4**a, 4d) and I (Figure S9-S10) atomic content are found similar on the bottom (long etching time) for both TMTA treated films, while higher elements content is found on the surface for TMTA post-treated film than the CSRC one, suggesting the accumulation of the excess PbI_2 on the surface for TMTA post-treated perovskite film, comparing to few excess PbI_2 on TMTA CSRC perovskite film surface. These unique distributions of Pb and I elements in the TMTA-treated films agree with the SEM and GIWAXS data. The binding energies at 143.58 and 138.78 eV are associated with Pb^{2+} $4f_{5/2}$ and $4f_{7/2}$, and the two shoulder peaks at 142.00 and 137.08 eV are attributed to the metallic Pb^0. The presence of Pb^0 is an indication of the existence of iodide vacancies in the perovskite lattice of the samples. The metallic Pb in the film is likely to act as non-radiative recombination centers that can impair solar cell operation.[38] The greatly reduced Pb^0 peaks in the TMTA CSRC film (Figure 4d) on the surface than the post-treated perovskite film (Figure 4a) is probably due to a lower level of iodide vacancies in the crystal lattice of the CSRC one.[39] The cross-linked TMTA at the perovskite grain boundary established a blocker for iodide mirgration[33, 40], leading to the lower level of iodide vacancies in the crystal lattice of the perovskite film. The lower level of iodide vacancies in CSRC film may result from the more efficient cross-linking of TMTA at the grain boundary through CSRC. The lower level of Pb defects can suppress the non-radiative recombination and enhance the PL lifetime, according to the TRPL results.

Figure 4b and 4e exhibit C1s spectra, where the 284.88 eV and 288.58 eV represent the C in C-C and C=O bonds, respectively. It is noted that both films present higher C1s

intensity of the C-C and C=O bond on the surface (more clearly shown in Figure S10), indicating the graded distribution of TMTA from the surface to the bottom layer. For the CSRC film, the O 1s signal (attributed to the ester group from TMTA (Figure 4c and 4f)) obviously shifts from 533 eV to 532 eV from the surface to the bottom due to the weak coordination with PbI_2, indicating the influence of TMTA varies with the film depth. The XPS results demonstrate that TMTA-CSRC takes part in the crystallization process of perovskite and reduces the iodide vacancies in the perovskite lattice, which is more significant when TMTA is located closer to the film surface. This will reduce the non-radiative recombination and contribute to better device performance by TMTA CSRC treatment.

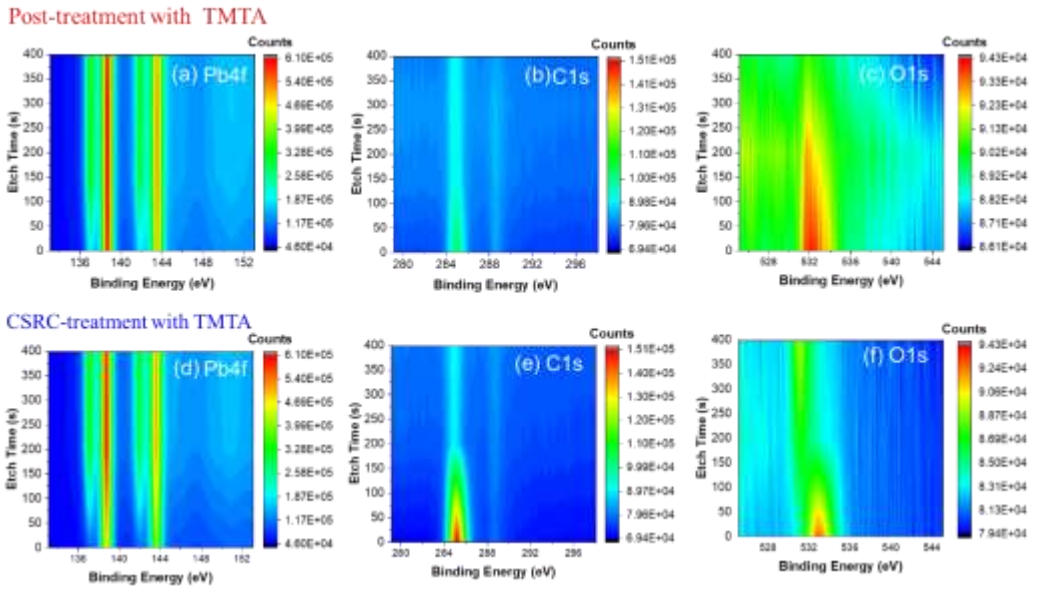

Figure 4. Elements XPS in-depth profiling of Pb, C, and O for perovskite films with TMTA post-treatment (a-c) and TMTA CSRC treatment (d-f).

To deep understand the perovskite formation mechanism with TMTA CSRC, PTMTA, induced by UV light and 150 ºC annealing process, i.e. the pre-cross-linked

TMTA, in CB antisolvent was applied as a comparison. As shown in **Figure 5**a, stage I and stage II refer to the intermediate perovskite phase and the annealing process for the complete perovskite film, respectively. The XRD patterns of perovskite films in stage I (Figure 5b) display 6H phase related peaks for all intermediate films[30, 41, 42]. There is negligible peak difference between control film, PTMTA and TMTA CSRC treated films. At stage II process, the α-$FAPbI_3$ phase formed (Figure 5c). The PTMTA treated film exhibits a similar XRD pattern with the control one, while displays weaker diffracted intensities of PbI_2 and δ-phase $FAPbI_3$ peaks, and a much low peak intensity at 24° (111) than that of the TMTA in CB one, indicating crystal preferred orientation in PTMTA in CB case. This is similar to the function of PMMA in anti-solvent in the former report[43]. The TMTA CSRC film however shows a significantly enhanced peak intensity at (111) facet. Considering PTMTA is just crosslinked TMTA, this indicates the enhanced crystal (111) facet should be linked to the *in situ* crosslinking process.

The morphology of the intermediate perovskite phase (stage I) illustrated in Figure 5d, presents uncovered and randomly distributed area in sheets formed for the control and PTMTA treated films, while for the TMTA treated one, the film has much better coverage and homogeneity. Hence, the TMTA is expected to uniformly trigger heterogeneous nucleation over the perovskite precursor film at stage I, and enhance the grain size at stage II via *in situ* cross-linking, which will benefit both the device performance and long-term stability of PSCs. It is noted that the PTMTA-treated perovskite films (stage II) present a mass of PTMTA nanoparticles on the surface of perovskite grain (Figure S11).

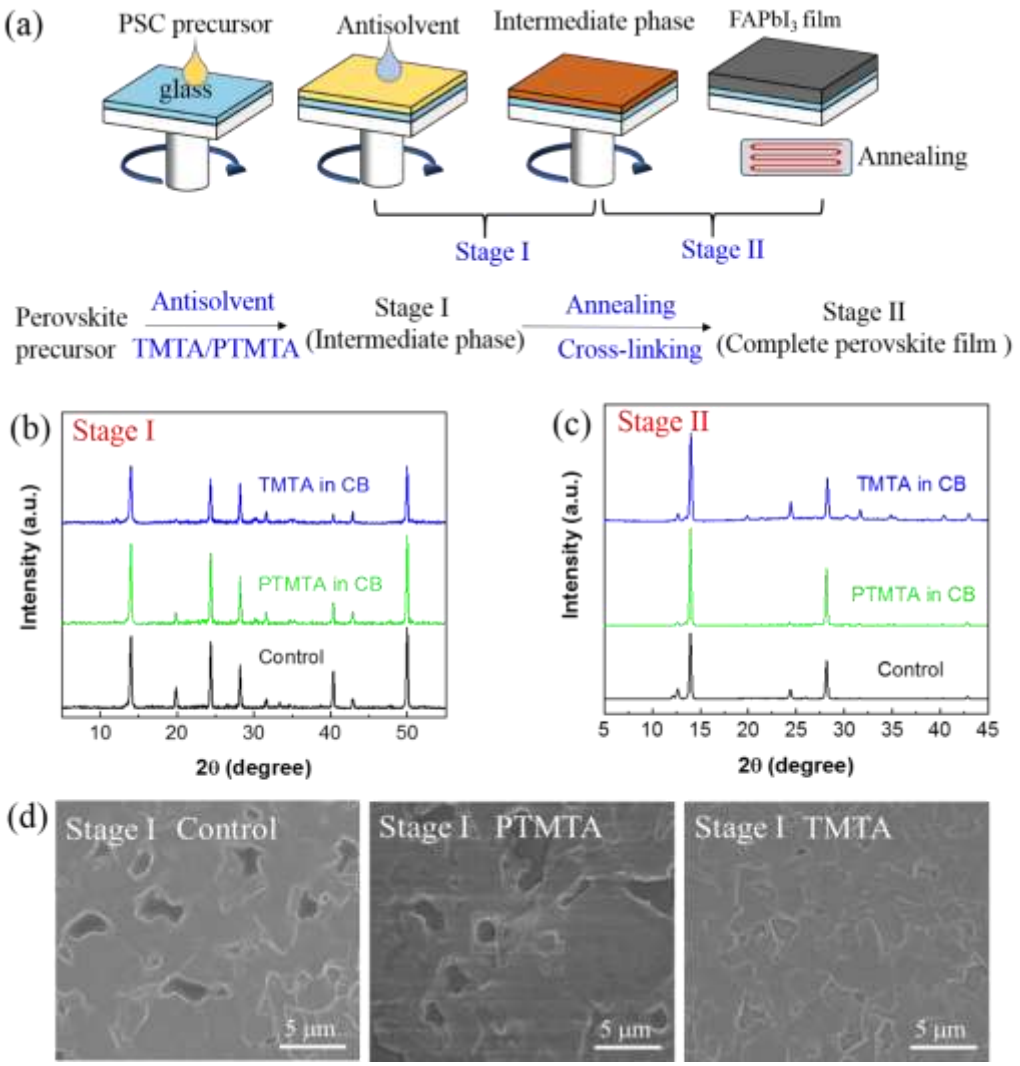

Figure 5. (a) The schematic illustration of two stages of perovskite formation kinetic with TMTA CSRC-treatment. The XRD patterns of control, PTMTA, and TMTA treated films for (b) stage I and (c) stage II. (d) SEM images of intermediate perovskite films treated with PTMTA or TMTA.

As well-known from recent studies, residual tensile strain (σ) existed in perovskite films is a critical source of intrinsic PSCs instability. Here we investigated the strain in perovskite films by grazing incident X-ray diffraction (GIXRD) technique with 2θ-$\sin^2\psi$ method. The plane (012) at 31.6° is selected for strain analysis due to its high multiplicity, which is generally adopted to acquire more grain information and alleviate

orientation effect on the linear relationship of 2θ-$\sin^2\psi$ in the GIXRD measurement. The XRD peaks for the control, PTMTA antisolvent-treated, and TMTA post-treated films gradually shift to the smaller 2θ (**Figure 6**a-6c), indicating the increase of crystal plane distance $d_{(012)}$ and the tensile strain bearing in these films. However, the scattering peak of TMTA CSRC-treated film gradually shifted to the larger 2θ (Figure 6d), suggesting that the TMTA CSRC-treated perovskite film is bearing compression strain. In general, perovskite film stress (σ) can be calculated by fitting 2θ as a function of $\sin^2\psi$[44], and the magnitude of residual strain can be reflected by the slope of the fitted line. The negative slope indicates the films bear tension stress. The slopes of the linear fit of 2θ-$\sin^2\psi$ for the control, TMTA post-treated, and PTMTA antisolvent-treated films are negative values, while it changes to a positive value for the TMTA CSRC film (Figure 6e). During the submission of this paper, Annalisa Bruno also found the existence of tensile stress in antisolvent treated perovskite film which is consistent with our results[45]. The already cross-linked PTMTA case has the same negative slope as the control, indicating little effect on the residual strain. The TMTA post-treated film on the surface can release the residual tensile strain to a certain extent, according to the slightly lower slope of linear fitted 2θ-$\sin^2\psi$. For the different TMTA concentrations in CSRC cases, the slopes are positive values (Figure 6f), implying the residual strain in TMTA CSRC films becomes compressive instead.

To demonstrate the general of CSRC method other than TMTA, four other types of cross-linking materials are applied for the strain characterization: trimethylolpropane ethoxylate triacrylate (ETPTA), 2-hydroxyethyl Methacrylate (HEMA), methyl

acrylate, acrylate acid (Figure S12). All these materials used for CSRC-treated perovskite films show compressive strain. Therefore, the universality of the proposed CSRC approach is identified. It is noted that the cross-linking process of TMTA is initialized under thermal annealing and TMTA is in the liquid phase before cross-linking. With the increasing concentration of TMTA, the slopes of linear fitted 2θ-$\sin^2\psi$ gradually increase, indicating that the film experiences a transition from tensile strain in the control film to strain-free and then to compression strain (Figure 6g). Based on these results, we find the strategy of regulating the film strain through the chemical cross-linking during the crystallization (TMTA in CB) is much more effective than post-treatment of the already-formed perovskite film (TMTA in IPA). We proposed the following scenario in explaining the experimental phenomena: It's well-known that the antisolvent dropping will form a large number of nuclei, a certain fraction which is bonded with TMTA molecules introduced in the CB, through coordination with Pb ions in the precursor, as confirmed by Fourier transform infrared spectroscopy (FTIR, Figure S13). The stretching vibration of C=O bond in pure TMTA appears at 1,730 cm^{-1}, while it shifts to 1,715 cm^{-1} upon interaction with PbI_2, indicating a weakened C=O bond strength caused by interaction with the Lewis acid PbI_2[34]. During the annealing perovskite crystal growth/formation process, the perovskite nuclei bonded with TMTA molecules cross-link with each other during the same annealing, providing compression confinement which balances the overall crystal thermal expansion. The molecule cross-linking compression also "pulls" adjacent small perovskite grains together, facilitate them to merge into larger perovskite grains. This explains the much larger perovskite

grain size in the CSRC approach. For the case of post-treatment, the TMTA mainly enters the grain boundary of the already-formed perovskite film, and cannot regulate strain in the most critical crystallization stage. Therefore, the post-treatment was a strain compensation strategy in nature, and the CSRC method is much more effective in releasing the perovskite residual tensile strain, even producing compression strain, and thus greatly enhances the intrinsic perovskite stability (shown in the following section).[25] It is noted that in the CSRC method, the TMTA is graded distributed from the surface to the bottom perovskite film as the XPS results demonstrated. The gradient distribution of TMTA is perfect matched and regulate the inhomogeneous residual stress distribution of perovskite film (top region-the largest lattice distortion).[18, 20, 46]

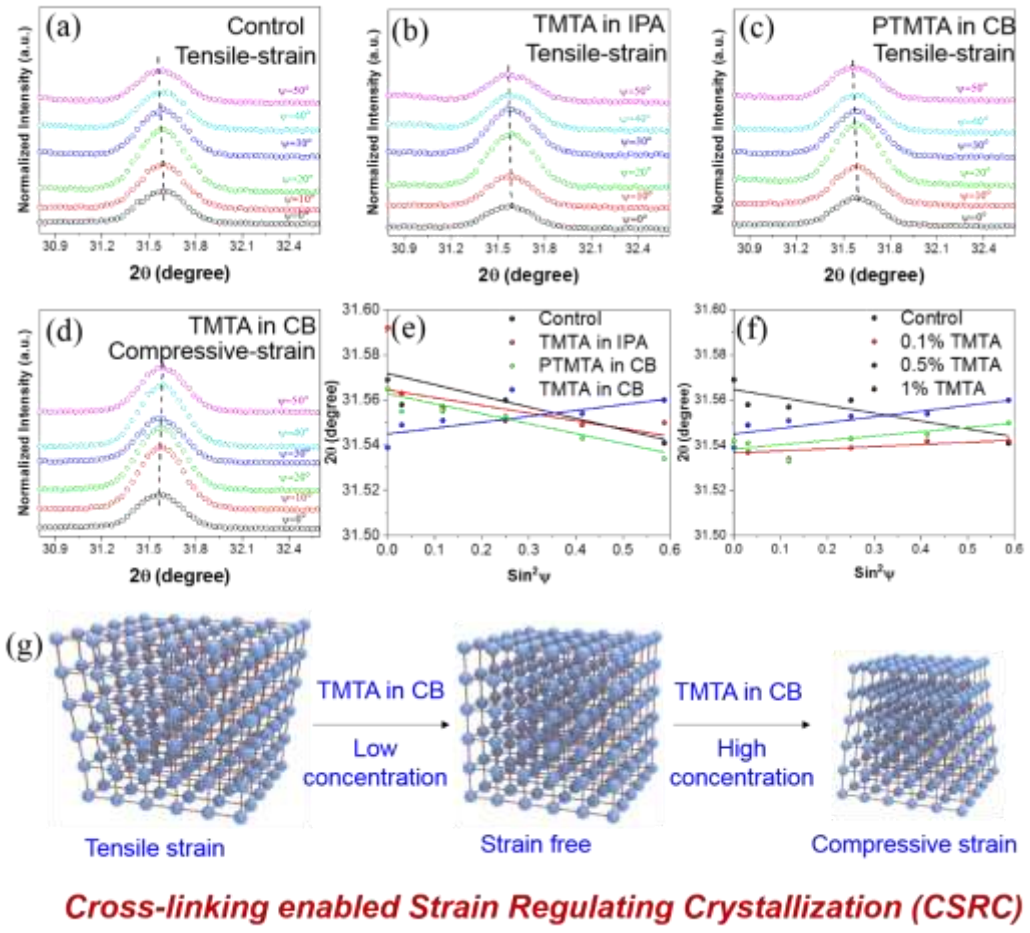

Figure 6. GIXRD with different instrumental ψ values (10°-50°) for (a) control film, (b) TMTA post-treated, (c) PTMTA antisolvent-treated and (d) TMTA CSRC-treated films. (e) Linear fit of 2θ-$\sin^2\psi$ for the test films with different TMTA treatment. (f) Linear fit of 2θ-$\sin^2\psi$ for the TMTA CSRC-treated films with TMTA in different concentrations. (g) The schematic representation of the tensile strain state of the control PSC film regulated by CSRC method with TMTA in different concentrations.

A detailed investigation of the device stability was then conducted on the PSCs (**Figure 7**). For the storage-stability (Figure 7a), the non-encapsulated devices were stored in a dark dry box with 20~30% relative humidity at room temperature. Compared to the control cells which maintain ~74% of its initial PCE after 4000 h storage, the TMTA post-treated and CSRC-treated devices retain 91% and 95% of their initial PCEs, respectively. The enhanced storage stability for non-encapsulated devices is attributed to the good waterproof property of the polymerized-TMTA protection layer on perovskite film. The TMTA CSRC films exhibited enhanced hydrophobicity (with water contact angles of 35.5°, 53.2°, 56.9° and 68.6° for TMTA CSRC perovskite films with 0.1%, 0.3%, 0.5% and 1% TMTA, respectively) over control perovskite film (27.5°). (Figure S14). The time evolution of water droplet (5 *ul*) on the control and CSRC treated films (Figure S15) clearly showed that the water droplets spread out very fast in several seconds for the control one, while the shapes of droplets on TMTA CSRC films maintained well for a relatively long time (several hours). When the droplets dried up after 5 h, the control film was severely damaged, and the damaged area of TMTA

treated films were well confined at the initial coating region, indicating lateral diffusion is effectively prohibited.[47] With the time going on (72 h and 144 h), the control film was almost damaged to the yellow phase while the CSRC films remained black, identifying the good stability of CSRC films under ambient environment (RH: 50~60%).

As for thermal stability (**Figure 7**b, at 80 °C in the N_2 filled glove box), after 950 h, the TMTA CSRC devices exhibited the best thermal stability (76% of its initial PCE) over the post-treatment (64% of its initial PCE) and control cases (59% of its initial PCE). The light stability results were obtained by exposing the encapsulated devices under a white light-emitting diode array with equivalent 0.8 sun AM 1.5G in the air (**Figure 7**c). In contrast to the rapid decrease of the control and TMTA post-treated devices, the TMTA CSRC PSCs demonstrated excellent light stability, maintaining 80% of its initial PCE after 1248 h. The excellent light stability of the TMTA CSRC device was attributed to the release of residual tensile through the strategy of *in situ* chemical cross-linking, which confines the crystal thermal expansion during the crystallization process.

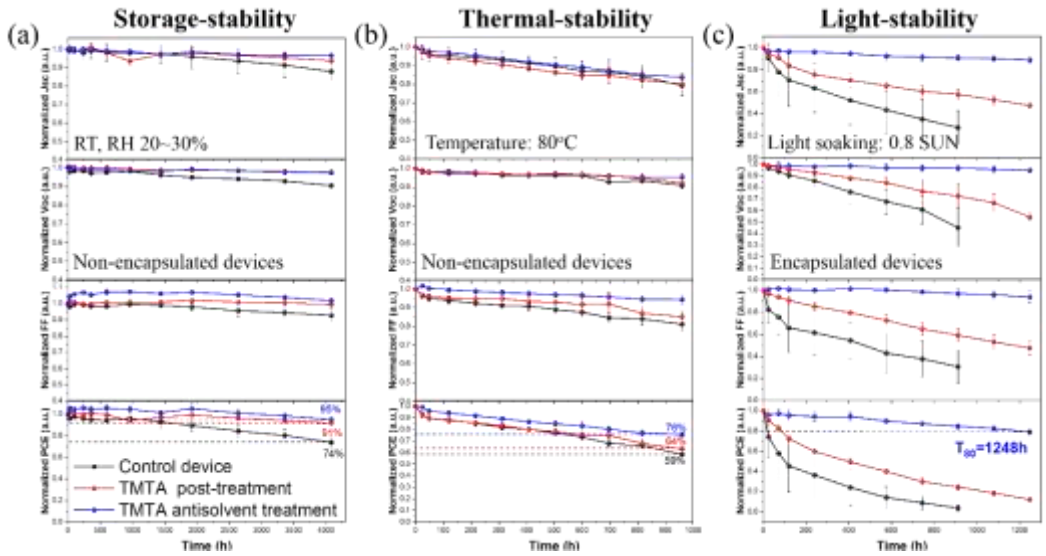

Figure 7. Stability of the control, TMTA post-treated, and TMTA CSRC-treated devices kept at (a) dry box with 20~30% relative humidity at room temperature (storage-stability); (b) 80 °C in glove box (thermal-stability); and (c) irradiation under a white light-emitting diode array with equivalent 0.8 sun AM 1.5G (light-stability). The error bars represent the standard deviation for 5 samples in each condition.

Conclusion

In summary, we have introduced a novel strain regulating strategy – CSRC, to precisely modulate the α-$FAPbI_3$-based film through synchronous cooperation of *in situ* TMTA chemical cross-linking and perovskite crystallization. The CSRC approach enables high quality α-$FAPbI_3$ film exhibiting multiple functionalities simultaneously, including strain regulation, humidity repulsion, reduced trap density, suppressed trap-assisted recombination, and enlarged grain size, leading to a remarkable 50 mV enhancement in V_{OC} and PCE increased to 22.39%. The CSRC enabled PSCs also exhibited superior stability: long-term stability of 95% of the initial PCE after 4000 h, and light-stability remaining 80% of the initial PCE after 1248 h. The CSRC approach provides a synergetic boost to PSC stability and efficiency, which is expected to be valuable for future PSC research.

References

1. Kim, H.-S.; Lee, C.-R.; Im, J.-H.; Lee, K.-B.; Moehl, T.; Marchioro, A.; Moon, S.-J.; Humphry-Baker, R.; Yum, J.-H.; Moser, J. E.; Grätzel, M.; Park, N.-G., Lead Iodide Perovskite Sensitized All-Solid-State Submicron Thin Film Mesoscopic Solar Cell with Efficiency Exceeding 9%. *Scientific Reports* **2012,** *2* (1), 591.

2. Park, N.-G.; Zhu, K., Scalable fabrication and coating methods for perovskite solar cells and solar modules. *Nature Reviews Materials* **2020**, 1-18.

3. Lee, M. M.; Teuscher, J.; Miyasaka, T.; Murakami, T. N.; Snaith, H. J., Efficient hybrid solar cells based on meso-superstructured organometal halide perovskites. *Science* **2012,** *338* (6107), 643-647.
4. Green, M. A.; Ho-Baillie, A.; Snaith, H. J., The emergence of perovskite solar cells. *Nature photonics* **2014,** *8* (7), 506-514.
5. Saliba, M.; Matsui, T.; Seo, J.-Y.; Domanski, K.; Correa-Baena, J.-P.; Nazeeruddin, M. K.; Zakeeruddin, S. M.; Tress, W.; Abate, A.; Hagfeldt, A., Cesium-containing triple cation perovskite solar cells: improved stability, reproducibility and high efficiency. *Energy & environmental science* **2016,** *9* (6), 1989-1997.
6. Saliba, M.; Matsui, T.; Domanski, K.; Seo, J.-Y.; Ummadisingu, A.; Zakeeruddin, S. M.; Correa-Baena, J.-P.; Tress, W. R.; Abate, A.; Hagfeldt, A., Incorporation of rubidium cations into perovskite solar cells improves photovoltaic performance. *Science* **2016,** *354* (6309), 206-209.
7. Zhou, H.; Chen, Q.; Li, G.; Luo, S.; Song, T.-b.; Duan, H.-S.; Hong, Z.; You, J.; Liu, Y.; Yang, Y., Interface engineering of highly efficient perovskite solar cells. *Science* **2014,** *345* (6196), 542-546.
8. Kojima, A.; Teshima, K.; Shirai, Y.; Miyasaka, T., Organometal halide perovskites as visible-light sensitizers for photovoltaic cells. *Journal of the American Chemical Society* **2009,** *131* (17), 6050-6051.
9. Laboratory, N. R. E., NREL Solar Cell Efficiency Chart. **2020**.
10. Kim, G.; Min, H.; Lee, K. S.; Yoon, S. M.; Seok, S. I., Impact of strain relaxation on performance of α-formamidinium lead iodide perovskite solar cells. *Science* **2020,** *370* (6512), 108-112.
11. Jeong, M.; Choi, I. W.; Go, E. M.; Cho, Y.; Kim, M.; Lee, B.; Jeong, S.; Jo, Y.; Choi, H. W.; Lee, J., Stable perovskite solar cells with efficiency exceeding 24.8% and 0.3-V voltage loss. *Science* **2020,** *369* (6511), 1615-1620.
12. Jiang, Q.; Zhao, Y.; Zhang, X.; Yang, X.; Chen, Y.; Chu, Z.; Ye, Q.; Li, X.; Yin, Z.; You, J., Surface passivation of perovskite film for efficient solar cells. *Nature Photonics* **2019,** *13* (7), 460-466.
13. Min, H.; Kim, M.; Lee, S.-U.; Kim, H.; Kim, G.; Choi, K.; Lee, J. H.; Seok, S. I., Efficient, stable solar cells by using inherent bandgap of α-phase formamidinium lead iodide. *Science* **2019,** *366* (6466), 749.
14. Liu, F.; Marongiu, D.; Pau, R.; Sarritzu, V.; Wang, Q.; Lai, S.; Lehmann, A. G.; Quochi, F.; Saba, M.; Mura, A.; Bongiovanni, G.; Mattoni, A.; Caddeo, C.; Bosin, A.; Filippetti, A., Ag/In lead-free double perovskites. *EcoMat* **2020,** *2* (1), e12017.
15. Yang, G.; Zhang, H.; Li, G.; Fang, G., Stabilizer-assisted growth of formamdinium-based perovskites for highly efficient and stable planar solar cells with over 22% efficiency. *Nano Energy* **2019,** *63*, 103835.
16. Yang, W. S.; Park, B.-W.; Jung, E. H.; Jeon, N. J.; Kim, Y. C.; Lee, D. U.; Shin, S. S.; Seo, J.; Kim, E. K.; Noh, J. H., Iodide management in formamidinium-lead-halide–based perovskite layers for efficient solar cells. *Science* **2017,** *356* (6345), 1376-1379.
17. Xue, D. J.; Hou, Y.; Liu, S. C.; Wei, M.; Chen, B.; Huang, Z.; Li, Z.; Sun, B.; Proppe, A. H.; Dong, Y.; Saidaminov, M. I.; Kelley, S. O.; Hu, J. S.; Sargent, E. H., Regulating strain in perovskite thin films through charge-transport layers. *Nat. Commun.* **2020,** *11* (1), 1514.
18. Zhao, J.; Deng, Y.; Wei, H.; Zheng, X.; Yu, Z.; Shao, Y.; Shield, J. E.; Huang, J., Strained

hybrid perovskite thin films and their impact on the intrinsic stability of perovskite solar cells. *Science advances* **2017,** *3* (11), eaao5616.

19. Rolston, N.; Bush, K. A.; Printz, A. D.; Gold‐Parker, A.; Ding, Y.; Toney, M. F.; McGehee, M. D.; Dauskardt, R. H., Engineering stress in perovskite solar cells to improve stability. *Advanced Energy Materials* **2018,** *8* (29), 1802139.

20. Wang, H.; Zhu, C.; Liu, L.; Ma, S.; Liu, P.; Wu, J.; Shi, C.; Du, Q.; Hao, Y.; Xiang, S.; Chen, H.; Chen, P.; Bai, Y.; Zhou, H.; Li, Y.; Chen, Q., Interfacial Residual Stress Relaxation in Perovskite Solar Cells with Improved Stability. *Adv. Mater.* **2019,** *31* (48), e1904408.

21. Zhu, C.; Niu, X.; Fu, Y.; Li, N.; Hu, C.; Chen, Y.; He, X.; Na, G.; Liu, P.; Zai, H.; Ge, Y.; Lu, Y.; Ke, X.; Bai, Y.; Yang, S.; Chen, P.; Li, Y.; Sui, M.; Zhang, L.; Zhou, H.; Chen, Q., Strain engineering in perovskite solar cells and its impacts on carrier dynamics. *Nat. Commun.* **2019,** *10* (1), 815.

22. Zhang, C.; Wu, S.; Tao, L.; Arumugam, G. M.; Liu, C.; Wang, Z.; Zhu, S.; Yang, Y.; Lin, J.; Liu, X.; Schropp, R. E. I.; Mai, Y., Fabrication Strategy for Efficient 2D/3D Perovskite Solar Cells Enabled by Diffusion Passivation and Strain Compensation. *Advanced Energy Materials* **2020,** *10* (43), 2002004.

23. Bush, K. A.; Rolston, N.; Gold‐Parker, A.; Manzoor, S.; Hausele, J.; Yu, Z. J.; Raiford, J. A.; Cheacharoen, R.; Holman, Z. C.; Toney, M. F., Controlling thin‐film stress and wrinkling during perovskite film formation. *ACS Energy Letters* **2018,** *3* (6), 1225‐1232.

24. Chen, B.; Rudd, P. N.; Yang, S.; Yuan, Y.; Huang, J., Imperfections and their passivation in halide perovskite solar cells. *Chem Soc Rev* **2019,** *48* (14), 3842‐3867.

25. Yang, N.; Zhu, C.; Chen, Y.; Zai, H.; Wang, C.; Wang, X.; Wang, H.; Ma, S.; Gao, Z.; Wang, X.; Hong, J.; Bai, Y.; Zhou, H.; Cui, B.‐B.; Chen, Q., In‐situ Cross‐linked 1D/3D Perovskite Heterostructure Improves Stability of Hybrid Perovskite Solar Cells for Over 3000h Operation. *Energy Environ. Sci.* **2020,** *13*, 4344‐4352.

26. Tai, Q.; Cao, J.; Wang, T.; Yan, F., Recent advances toward efficient and stable tin‐based perovskite solar cells. *EcoMat* **2019,** *1* (1), e12004.

27. Kundu, S.; Kelly, T. L., In situ studies of the degradation mechanisms of perovskite solar cells. *EcoMat* **2020,** *2* (2), e12025.

28. Qin, M.; Xue, H.; Zhang, H.; Hu, H.; Liu, K.; Li, Y.; Qin, Z.; Ma, J.; Zhu, H.; Yan, K., Precise Control of Perovskite Crystallization Kinetics via Sequential A‐Site Doping. *Advanced Materials* **2020,** *32* (42), 2004630.

29. Niu, T.; Lu, J.; Munir, R.; Li, J.; Barrit, D.; Zhang, X.; Hu, H.; Yang, Z.; Amassian, A.; Zhao, K., Stable high‐performance perovskite solar cells via grain boundary passivation. *Advanced Materials* **2018,** *30* (16), 1706576.

30. Niu, T.; Lu, J.; Tang, M.‐C.; Barrit, D.; Smilgies, D.‐M.; Yang, Z.; Li, J.; Fan, Y.; Luo, T.; McCulloch, I., High performance ambient‐air‐stable FAPbI 3 perovskite solar cells with molecule‐passivated Ruddlesden–Popper/3D heterostructured film. *Energy & Environmental Science* **2018,** *11* (12), 3358‐3366.

31. Li, X.; Zhang, W.; Wang, Y.‐C.; Zhang, W.; Wang, H.‐Q.; Fang, J., In‐situ cross‐linking strategy for efficient and operationally stable methylammoniun lead iodide solar cells. *Nature communications* **2018,** *9* (1), 1‐10.

32. Li, X.; Fu, S.; Liu, S.; Wu, Y.; Zhang, W.; Song, W.; Fang, J., Suppressing the ions‐induced degradation for operationally stable perovskite solar cells. *Nano Energy* **2019,** *64*, 103962.

33. Li, X.; Zhang, W.; Wang, Y. C.; Zhang, W.; Wang, H. Q.; Fang, J., In-situ cross-linking strategy for efficient and operationally stable methylammoniun lead iodide solar cells. *Nat Commun* **2018,** *9* (1), 3806.
34. Han, T. H.; Lee, J. W.; Choi, C.; Tan, S.; Lee, C.; Zhao, Y.; Dai, Z.; De Marco, N.; Lee, S. J.; Bae, S. H.; Yuan, Y.; Lee, H. M.; Huang, Y.; Yang, Y., Perovskite-polymer composite cross-linker approach for highly-stable and efficient perovskite solar cells. *Nat Commun* **2019,** *10* (1), 520.
35. Wang, H.; Wang, Z.; Yang, Z.; Xu, Y.; Ding, Y.; Tan, L.; Yi, C.; Zhang, Z.; Meng, K.; Chen, G., Ligand-Modulated Excess PbI2 Nanosheets for Highly Efficient and Stable Perovskite Solar Cells. *Advanced Materials* **2020,** *32* (21), 2000865.
36. Liu, K.; Liang, Q.; Qin, M.; Shen, D.; Yin, H.; Ren, Z.; Zhang, Y.; Zhang, H.; Fong, P. W.; Wu, Z., Zwitterionic-Surfactant-Assisted Room-Temperature Coating of Efficient Perovskite Solar Cells. *Joule* **2020,** *4* (11), 2404-2425.
37. Yu, W.; Yu, S.; Zhang, J.; Liang, W.; Wang, X.; Guo, X.; Li, C., Two-in-one additive-engineering strategy for improved air stability of planar perovskite solar cells. *Nano Energy* **2018,** *45*, 229-235.
38. Qin, M.; Cao, J.; Zhang, T.; Mai, J.; Lau, T. K.; Zhou, S.; Zhou, Y.; Wang, J.; Hsu, Y. J.; Zhao, N., Fused-Ring Electron Acceptor ITIC-Th: A Novel Stabilizer for Halide Perovskite Precursor Solution. *Advanced Energy Materials* **2018,** *8* (18), 1703399.
39. Bi, D.; Yi, C.; Luo, J.; Décoppet, J.-D.; Zhang, F.; Zakeeruddin, Shaik M.; Li, X.; Hagfeldt, A.; Grätzel, M., Polymer-templated nucleation and crystal growth of perovskite films for solar cells with efficiency greater than 21%. *Nature Energy* **2016,** *1* (10), 16142.
40. Lindblad, R.; Bi, D.; Park, B.-w.; Oscarsson, J.; Gorgoi, M.; Siegbahn, H.; Odelius, M.; Johansson, E. M.; Rensmo, H. k., Electronic structure of TiO2/CH3NH3PbI3 perovskite solar cell interfaces. *The journal of physical chemistry letters* **2014,** *5* (4), 648-653.
41. Tang, M.-C.; Fan, Y.; Barrit, D.; Chang, X.; Dang, H. X.; Li, R.; Wang, K.; Smilgies, D.-M.; Liu, S. F.; De Wolf, S., Ambient blade coating of mixed cation, mixed halide perovskites without dripping: in situ investigation and highly efficient solar cells. *Journal of Materials Chemistry A* **2020,** *8* (3), 1095-1104.
42. Gratia, P.; Zimmermann, I.; Schouwink, P.; Yum, J.-H.; Audinot, J.-N.; Sivula, K.; Wirtz, T.; Nazeeruddin, M. K., The many faces of mixed ion perovskites: unraveling and understanding the crystallization process. *ACS Energy Letters* **2017,** *2* (12), 2686-2693.
43. Bi, D.; Yi, C.; Luo, J.; Décoppet, J.-D.; Zhang, F.; Zakeeruddin, S. M.; Li, X.; Hagfeldt, A.; Grätzel, M., Polymer-templated nucleation and crystal growth of perovskite films for solar cells with efficiency greater than 21%. *Nature Energy* **2016,** *1* (10), 1-5.
44. Wang, H.; Zhu, C.; Liu, L.; Ma, S.; Liu, P.; Wu, J.; Shi, C.; Du, Q.; Hao, Y.; Xiang, S., Interfacial residual stress relaxation in perovskite solar cells with improved stability. *Advanced Materials* **2019,** *31* (48), 1904408.
45. Dewi, H. A.; Li, J.; Wang, H.; Chaudhary, B.; Mathews, N.; Mhaisalkar, S.; Bruno, A., Excellent Intrinsic Long-Term Thermal Stability of Co-Evaporated MAPbI3 Solar Cells at 85° C. *Advanced Functional Materials* **2021**, 2100557.
46. Zhu, C.; Niu, X.; Fu, Y.; Li, N.; Hu, C.; Chen, Y.; He, X.; Na, G.; Liu, P.; Zai, H., Strain engineering in perovskite solar cells and its impacts on carrier dynamics. *Nature communications* **2019,** *10* (1), 1-11.

47. Qin, P. L.; Yang, G.; Ren, Z. w.; Cheung, S. H.; So, S. K.; Chen, L.; Hao, J.; Hou, J.; Li, G., Stable and Efficient Organo-Metal Halide Hybrid Perovskite Solar Cells via π-Conjugated Lewis Base Polymer Induced Trap Passivation and Charge Extraction. *Advanced Materials* **2018,** *30* (12), 1706126.

Acknowledgements:

G.L. would like to thank the support by Research Grants Council of Hong Kong (Grant No. 15246816, and C5037-18G), Shenzhen Science and Technology Innovation Commission (Project No. JCYJ20170413154602102), the Project of Strategic Importance (Project No. 1-ZE29), University Supporting Fund for Major Research (1-BBAS) and Sir Sze-yuen Chung Endowed Professorship Fund (8-8480) provided by the Hong Kong Polytechnic University. W.Y. would like to thank the support by DICP ZZBS201813.

Competing financial interests:

The authors declare no competing financial interests.

Data and materials availability:

All data needed to evaluate the conclusions in this paper are present in the paper and/or the supplementary materials. The data can be requested from G.L. and W.Y. (corresponding authors).

Supporting information

Multi-functional Cross-linking Enabled Strain Regulating Crystallization for Stable, Efficient α-$FAPbI_3$-based Perovskite Solar Cells

Hengkai Zhang[1,2], Zhiliang Chen[1], Minchao Qin[3], Zhiwei Ren[1,2], Kuan Liu[1,2], Jiaming Huang[1,2], Dong Shen[4], Zehan Wu[5], Yaokang Zhang[6], Jianhua Hao[5], Chun-sing Lee[4], Xinhui Lu[3], Zijian Zheng[6], Wei Yu[1,7], Gang Li[1,2*]*

[1]Department of Electronic and Information Engineering, Research Institute for Smart Energy (RISE), The Hong Kong Polytechnic University, Hung Hom, Kowloon, Hong Kong, China

[2]The Hong Kong Polytechnic University Shenzhen Research Institute, Shenzhen 518057, China

[3]Department of Physics, The Chinese University of Hong Kong, New Territories, Hong Kong, China

[4]Center of Super-Diamond and Advanced Films (COSDAF) and Department of Chemistry, City University of Hong Kong, Kowloon, Hong Kong, China

[5]Department of Applied Physics, The Hong Kong Polytechnic University, New Territories, Hong Kong, China

[6]Laboratory for Advanced Interfacial Materials and Devices, Research Centre for Smart Wearable Technology, Institute of Textiles and Clothing, The Hong Kong Polytechnic University, Hung Hom, Kowloon, Hong Kong, China

[7]State Key Laboratory of Catalysis, Dalian Institute of Chemical Physics, Chinese Academy of Sciences, Dalian National Laboratory for Clean Energy, Dalian 116023, Liaoning, China

* Correspondence author. Email: wyu@dicp.ac.cn (W.Y.); gang.w.li@polyu.edu.hk (G.L.)

Experimental section

Materials

Trimethylolpropane triacrylate (TMTA) and SnO_2 colloid precursor were purchased from Alfa Aesar. Formamidinium iodide (FAI), methylammonium bromide (MABr), and methylammonium chloride (MACl) were bought from Greatcell Energy. Lead iodide (PbI_2), N, N−dimethylformamide (DMF), and dimethyl sulfoxide (DMSO) were obtained from Sigma-Aldrich. Spiro-OMeTAD was from Lumtec. ITO glass was purchased from Advanced Election Technology Co., Ltd. All chemicals were used without any further purification process.

Device Fabrication

The ITO glass was cleaned in detergent, deionized water, acetone, and isopropyl alcohol sequentially. After dried by N_2 blowing, the cleaned ITO substrates were treated with ultraviolet ozone for 15 min to remove organic residues and enhance surface wetting. Then the prepared SnO_2 precursor (diluted by water with SnO_2:H_2O=1:4, v/v) was spin-coated onto the ITO substrate at 4000 rpm for 30 s, followed by thermal annealing at 150 °C for 30 min in ambient air. The ITO/SnO_2 samples were treated with

ultraviolet ozone for 10 min before deposition of perovskite film. The perovskite precursor $(FAPbI_3)_{0.95}(MAPbBr_3)_{0.05}$ with 889 mg mL^{-1} of $FAPbI_3$, 33 mg mL^{-1} $MAPbBr_3$, 10% excess of PbI_2 (64.5 mg mL^{-1}) and 33 mg mL^{-1} MACl in DMF/DMSO (8:1 v/v) solvent was then spin-coated onto ITO/SnO_2 by two consecutive spin-coating steps (1000 rpm 5 s and 5000 rpm 20 s). During the spin-coating process, the antisolvent of chlorobenzene or TMTA in chlorobenzene (CSRC-treatment) was poured onto the perovskite film at 15 s. The intermediate phase film was annealed under 150 ºC for 10 min in the glove box. For the post-treatment device, TMTA in isopropanol was spin-coated onto the perovskite film at 5000 rpm 30 s and annealed at 150 ºC for 10 min. Then, the hole transporting layer of 2,2′,7,7′−tetrakis(N, N−dip−methoxyphenylamine)−9,9′−spirobifluorene (Spiro−OMeTAD) was deposited onto the top of the perovskite layer by 3500 rpm for 30 s with the composition of 72.8 mg Spiro−OMeTAD, 18.8 µL bis(trifluoromethane) sulfonimide lithium salt (Li−TFSI) stock solution (520 mg Li−TFSI in 1 mL acetonitrile), 28.8 µL 4−tertbutylpyridine, and 1 mL chlorobenzene. Finally, 80 nm of Au film was thermally evaporated as a counter electrode using a shadow mask. For $FA_{0.93}MA_{0.04}Cs_{0.03}$-based PSCs, 1.4M $FAPbI_3$, 0.06M $MAPbBr_3$, and 0.045M $CsPbI_3$ and 0.5M MACl were dissolved in DMF/DMSO (8:1 v/v) solvent. The following spin-coating process and treatments were same with $(FAPbI_3)_{0.95}(MAPbBr_3)_{0.05}$ perovskite solar cell.

Characterizations and measurements

The current-voltage (*J-V*) characteristic and steady-state power output of

photovoltaic devices were measured by Keithley 2400 Source Meter under standard AM 1.5 G illumination using a solar simulator (Enli Tech, Taiwan), and the light intensity was calibrated by KG-5 silicon diode. The step voltage and scan speeds were 20 mV and 100 mV s^{-1}. EQE measurement was carried out with an EQE system (Enli Tech, Taiwan) using 100 Hz chopped monochromatic light ranging from 300 nm to 900 nm.

The XRD patterns of perovskite films were collected from Rigaku SmartLab X-ray diffractometer with Cu Kα radiation in a step of 0.01° and θ-2θ scan mode. The GIWAXS measurements were carried out with a Xeuss 2.0 SAXS/WAXS laboratory beamline using a Cu X-ray source (8.05 keV, 1.54 Å) and a Pilatus3R 300K detector. The incidence angle is 0.3°. The SEM images were collected from a field emission scanning electron microscope (Tescan MAIA3). The steady-state photoluminescence and time-resolved photoluminescence spectra were measured on the Edinburgh FLSP920 spectrophotometer equipped with the excitation source of 485 nm picosecond pulsed diode laser in the average power of 0.15 mW. The absorption spectra of perovskite films were measured by the UV-vis spectrophotometer (CARY5000, Varian). The X-ray photoelectron spectroscopy (XPS) was measured from the X-Ray photoelectron spectrometer system (Thermo scientific Nexsa) equipped with 12 kV aluminum Ka X-ray. The depth profiling XPS was achieved by an Ar^{+} gun beam to etch perovskite films and collected by XPS analyses.

Photo-stability was measured using encapsulated devices under a white light-emitting diode array with the intensity equally with 0.8 sun AM 1.5G, calibrated by a

standard silicon photodiode detector (equipped with KG-5 filter). For the thermal stability measurement, the PTAA layer was selected as the hole transporting layer by spin-coating of PTAA solution (10 mg mL^{-1} in toluene, 2 μL tBP, and 2 μL Li-TFSI solution-520 mg mL^{-1} in acetonitrile) onto perovskite film at 4000 rpm for 30 s.

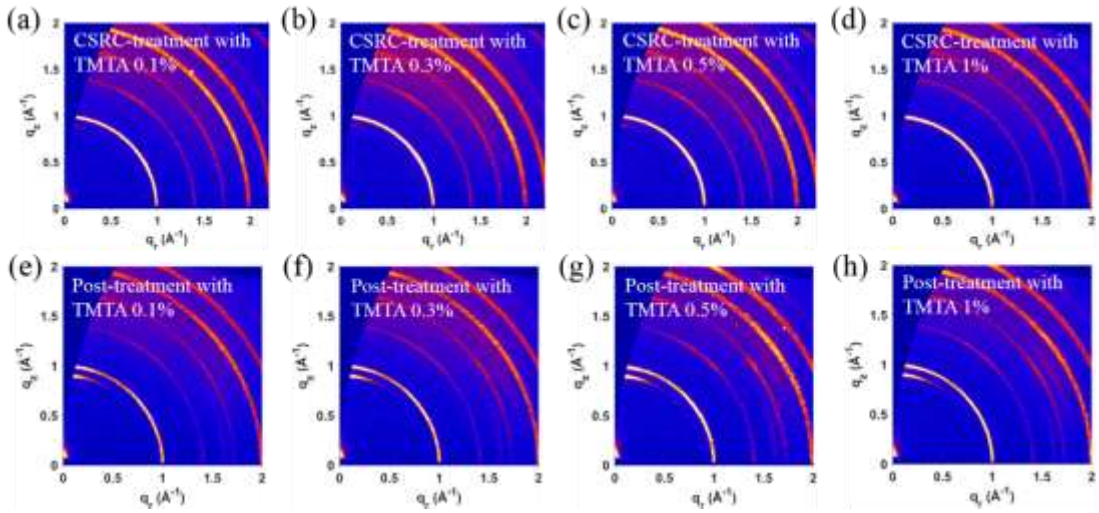

Figure S1. GIWAXS maps for perovskite films of CSRC-treatment with different concentrations of TMTA in CB (a-d), and of post-treatment with different concentrations of TMTA in IPA (e-h).

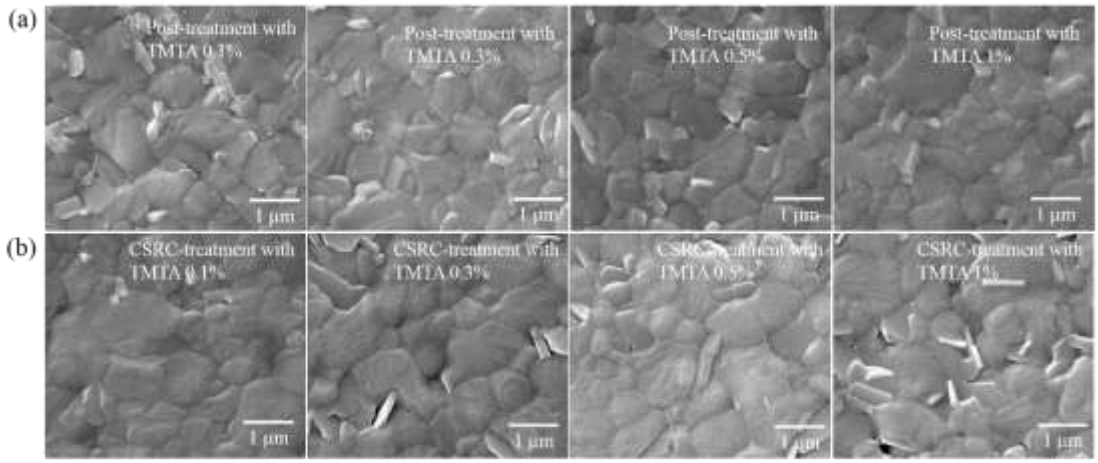

Figure S2. SEM images of (a) post-treatment of perovskite films with different concentrations of TMTA in IPA, and (b) CSRC-treatment of perovskite films with different concentrations of TMTA

in CB.

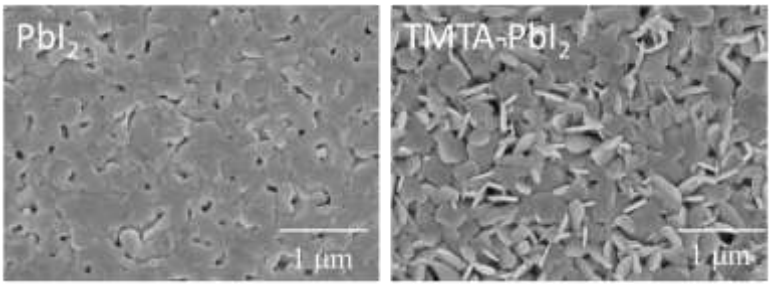

Figure S3. SEM images of PbI_2 and TMTA-PbI_2 films.

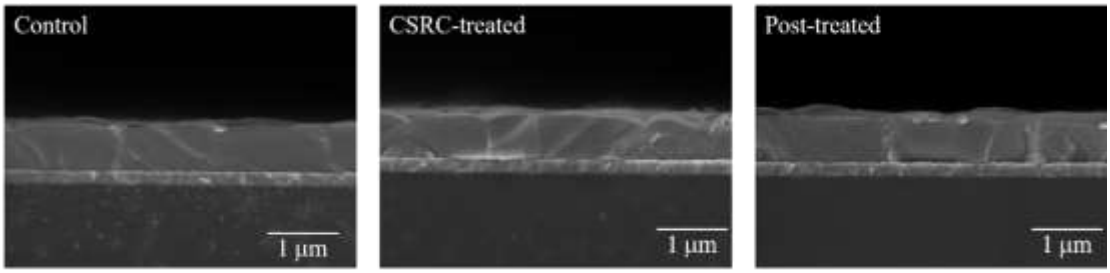

Figure S4. Cross-sectional SEM images of control, TMTA CSRC-treated and post-treated perovskite films.

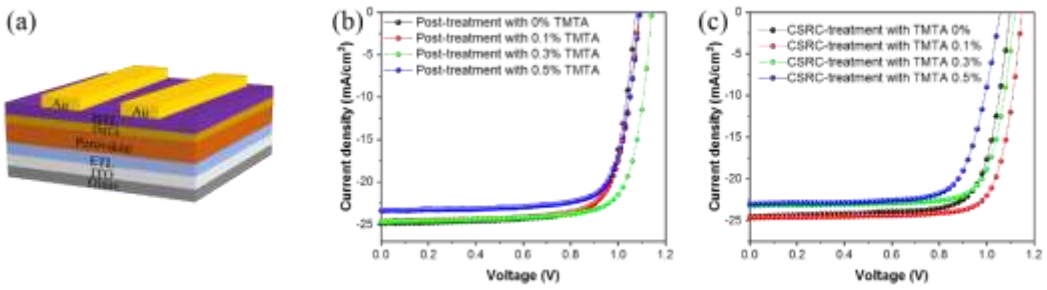

Figure S5. (a) Device structure of Glass/ITO/SnO_2/PSC/Spiro-OMeTAD/Au. *J-V* curves of PSCs with (b) TMTA post-treatment and (c) TMTA CSRC-treatment with different concentrations.

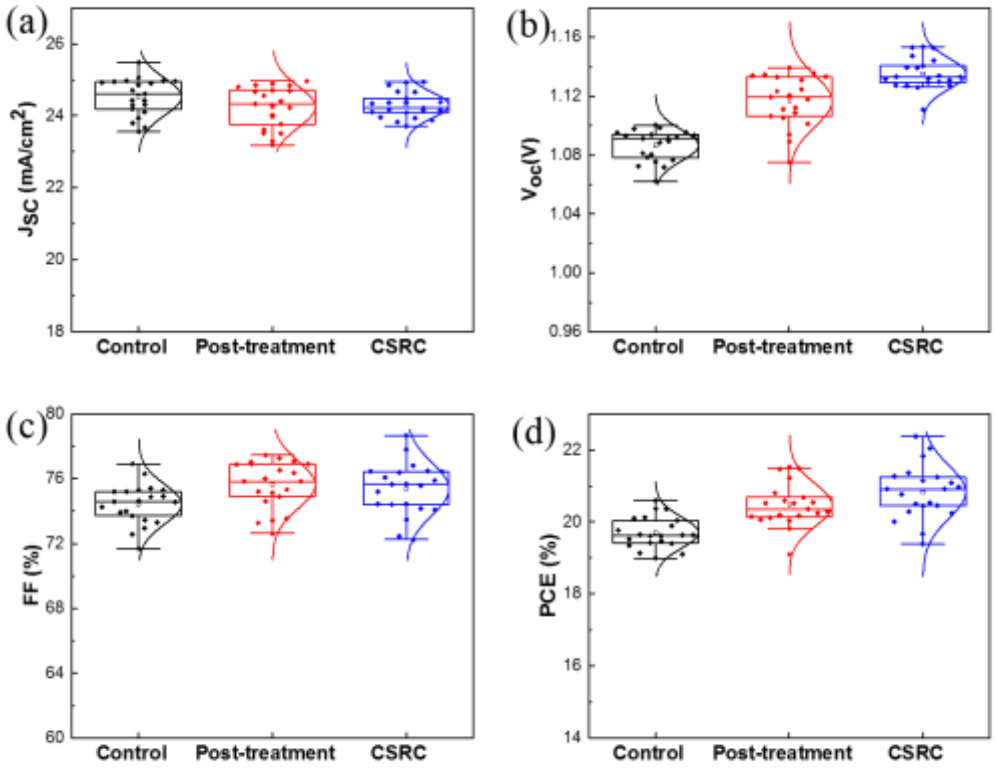

Figure S6. Statistical deviation of the photovoltaic parameters of (a) J_{SC}, (b) V_{OC}, (c) FF and (d) PCE for the control, TMTA post-treatment and TMTA CSRC-treatment devices (20 cells for each type).

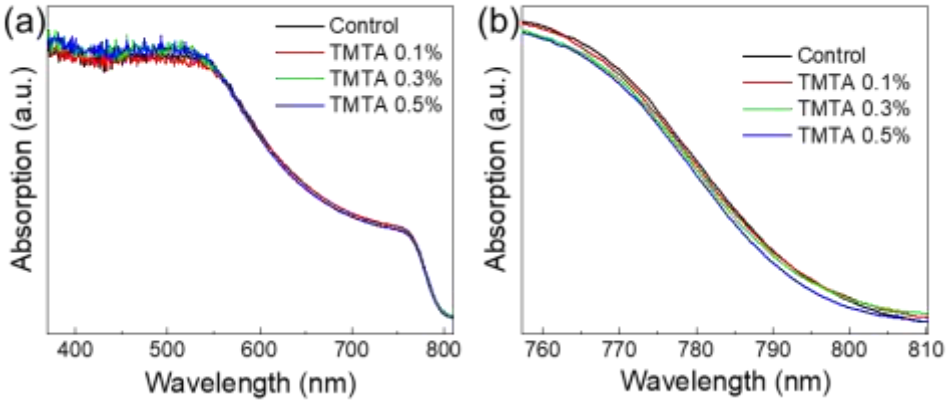

Figure S7. UV-vis absorption spectra of control and CSRC-treated perovskite films with different concentration of TMTA.

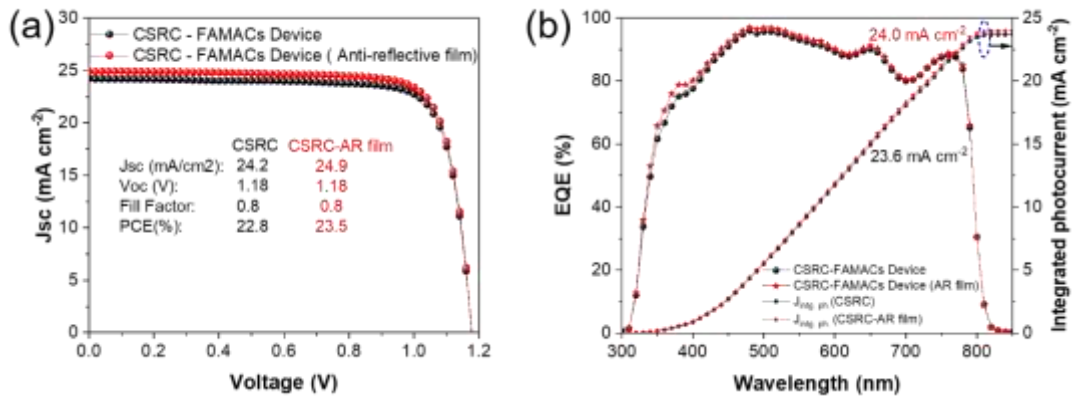

Figure S8. (a) The *J-V* curves and (b) EQE of CSRC-treated $FA_{0.93}MA_{0.04}Cs_{0.03}$ PSCs without and with Anti-reflective film.

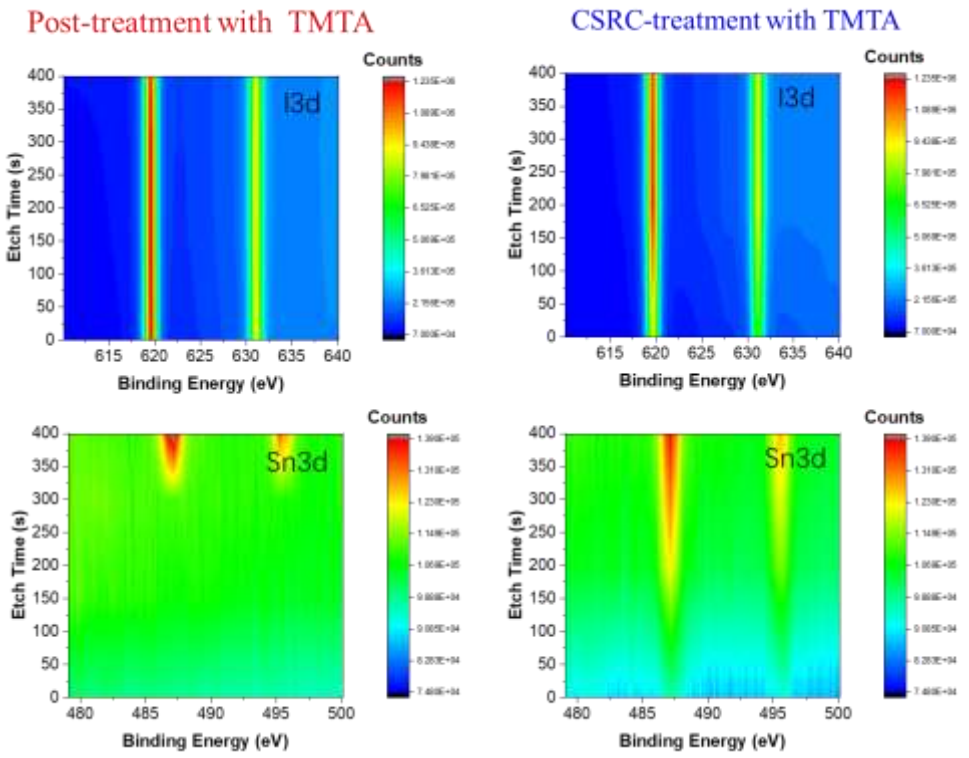

Figure S9. The I and Sn XPS in-depth profiling of perovskite films with TMTA post-treatment and TMTA CSRC-treatment.

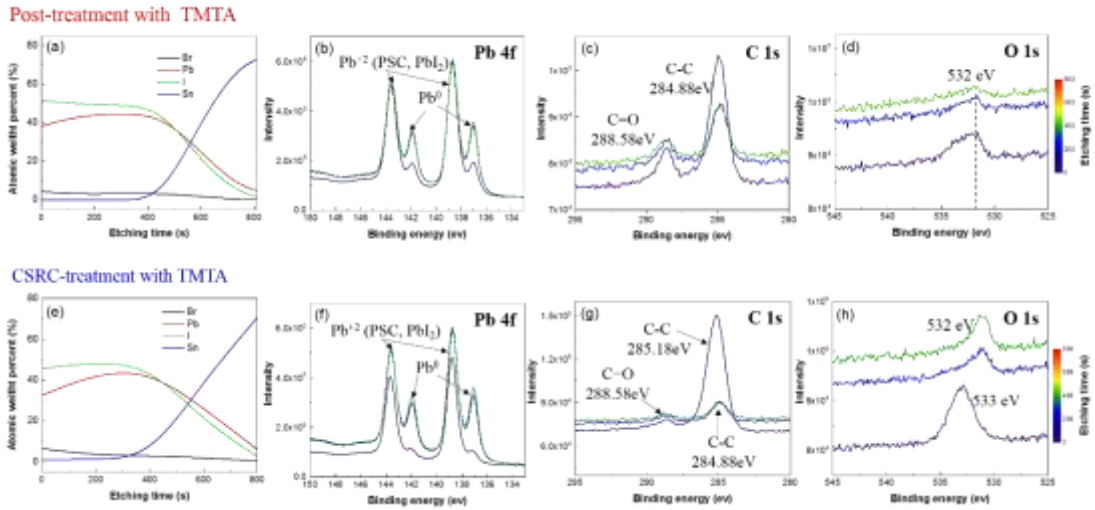

Figure S10. (a) XPS compositional profile of elected elements with different etching time and core level XPS spectra of (b) Pb 4f, (c) C 1s, and (d) O 1s spectra of perovskite film with TMTA post-treated. (e) XPS compositional profile of elected elements with different etching time and core level XPS spectra of (f) Pb 4f, (g) C 1s, and (h) O 1s spectra of perovskite film with TMTA CSRC-treatment.

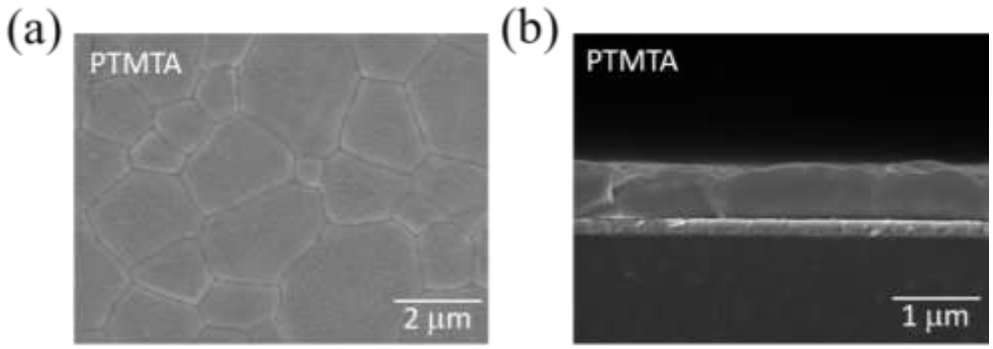

Figure S11. SEM images of PTMTA-treated perovskite films (Stage II). (a) top-view SEM image and (b) cross-sectional SEM image.

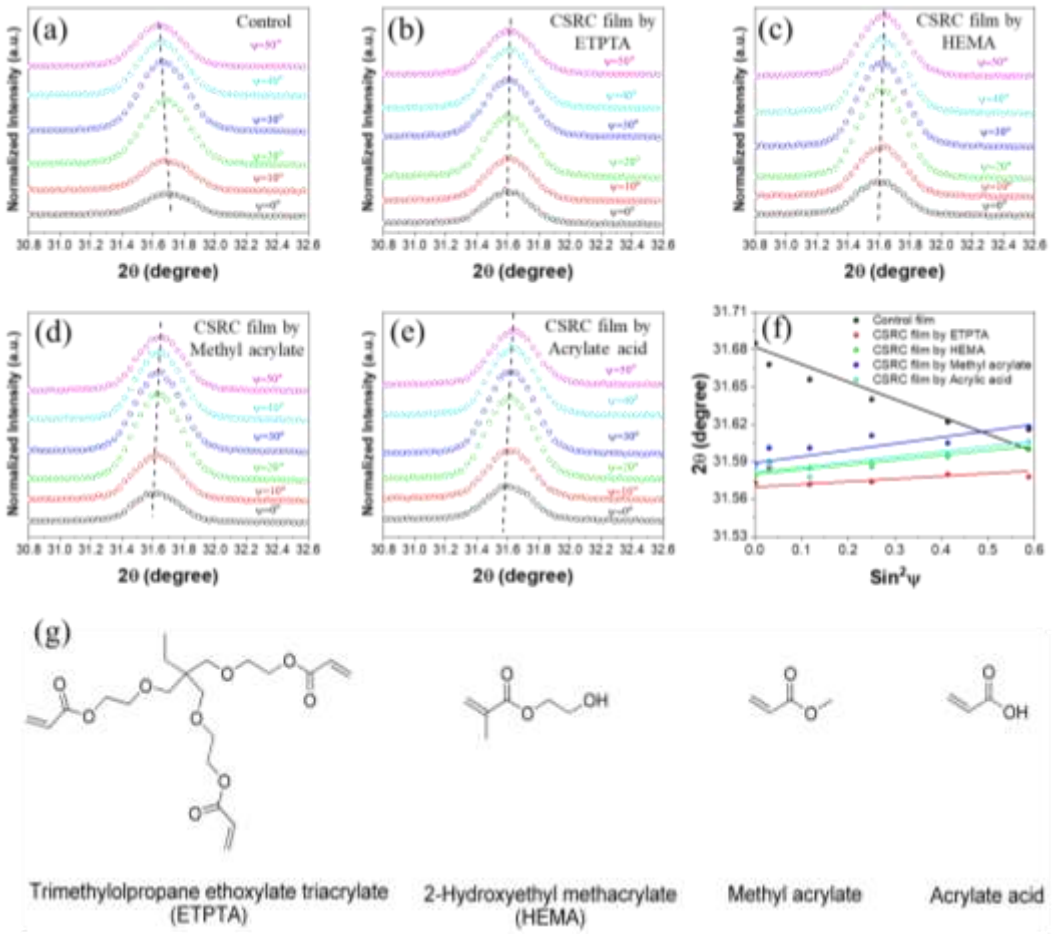

Figure S12. GIXRD with different instrumental ψ values (10°-50°) for (a) control film, (b-e) CSRC-treated perovskite films with ETPTA (trimethylolpropane ethoxylate triacrylate), HEMA (2-hydroxyethyl methacrylate), methyl acrylate, and acrylate acid, respectively. (f) Linear fit of 2θ-$\sin^2\psi$ for the test films with different materials treatment. (g) Chemical structures of ETPTA, HEMA, methyl acrylate and acrylate acid.

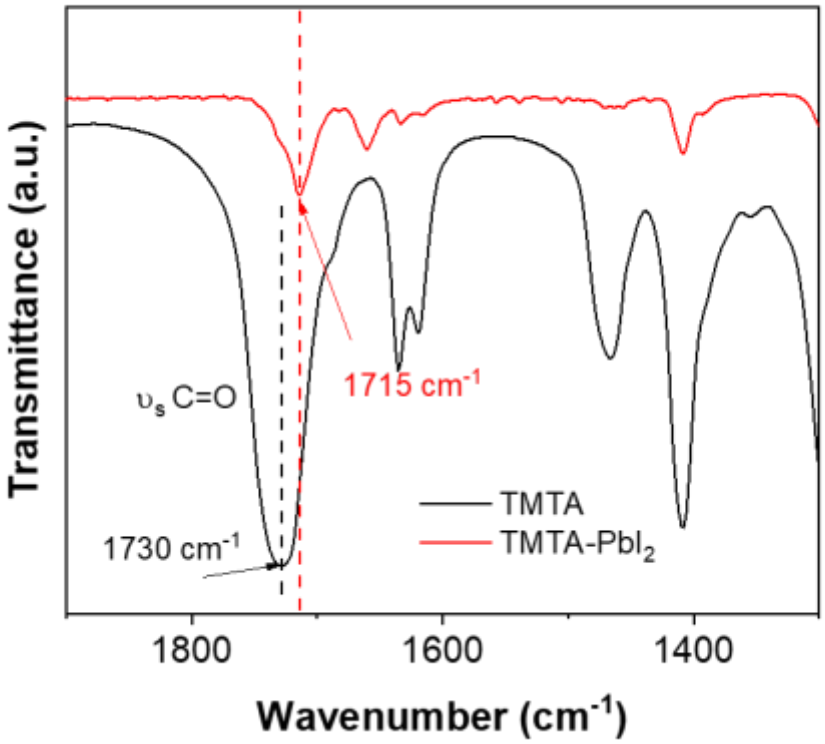

Figure S13. FTIR spectra of TMTA-PbI_2 prepared by mixing TMTA with PbI_2 and the pristine TMTA films.

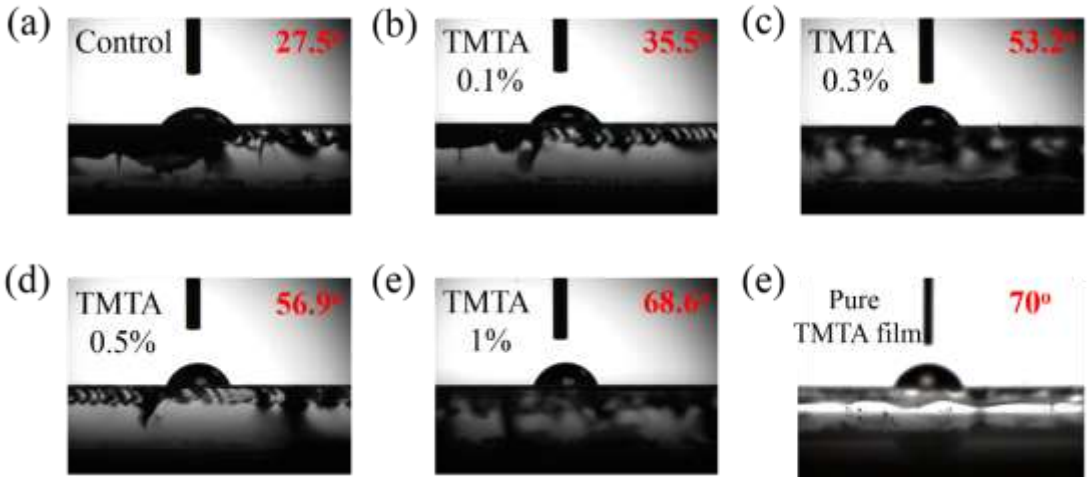

Figure S14. The static contact angles of deionized water on the top of (a) control film and films with CSRC-treatment of (b) 0.1% TMTA, (c) 0.3% TMTA, (d) 0.5% TMTA, (e) 1% TMTA, and (f) Pure TMTA-polymerization film.

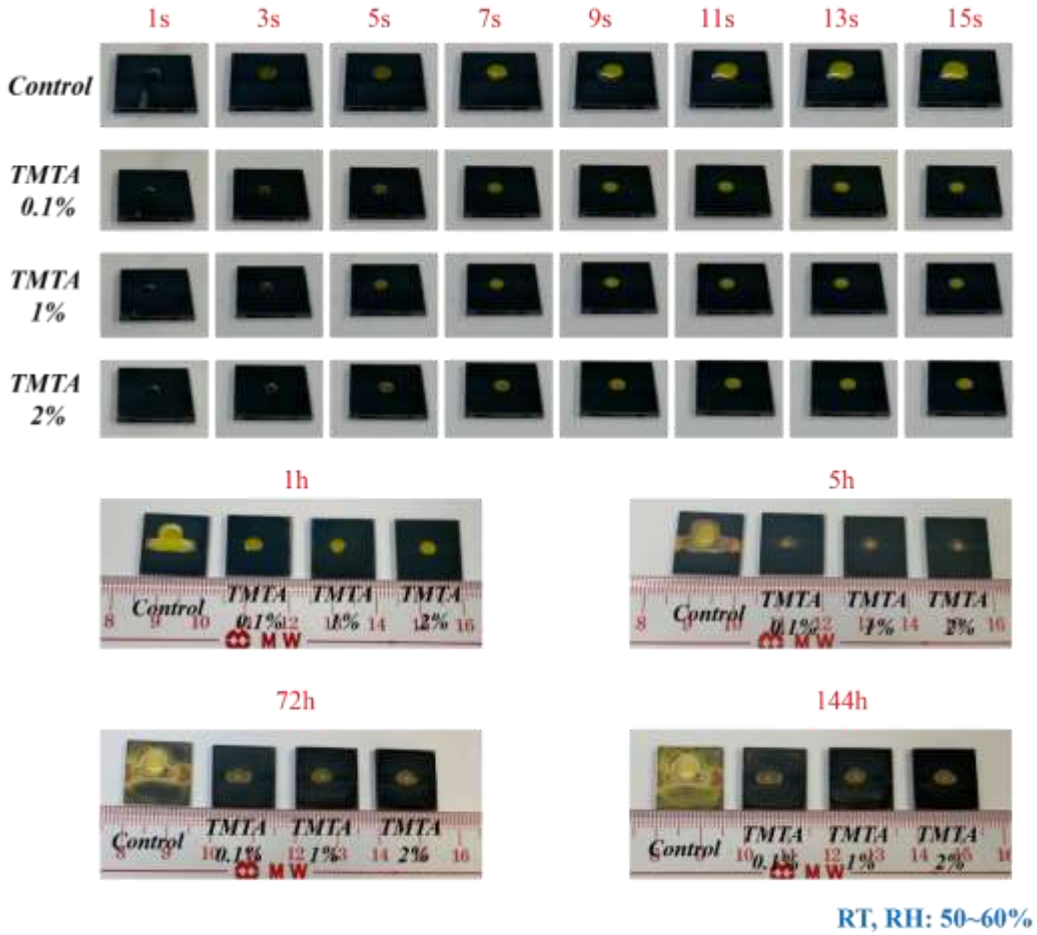

Figure S15. Time-evolution of the water drops on control film and film with TMTA CSRC-treatment.

Table S1. Photovoltaic parameters of PSCs with TMTA in different concentrations.

	V_{OC} (V)	J_{SC} (mA cm^{-2})	FF (%)	PCE(%)
Control	1.10	24.53	75.3	20.3
Surface post-treated				
0.1% TMTA	1.10	24.66	75.5	20.5
0.3% TMTA	1.14	24.80	76.6	21.7
0.5% TMTA	1.09	23.40	76.3	19.5
CSRC-treated				
0.1% TMTA	1.15	24.80	78.5	22.4
0.3% TMTA	1.12	23.30	77.0	20.0
0.5% TMTA	1.06	22.90	73.0	17.8

Table S2. Photovoltaic parameters determined from the *J-V* measurements of the PSCs based on TMTA post-treatment and CSRC-treatment.

Device		V_{OC} (V)	J_{SC} (mA cm^{-2})	FF (%)	PCE(%)	Hysteresis Index
control	Forward scan	1.08	24.37	74.7	19.7	0.030
	Reverse scan	1.10	24.5	75.3	20.3	
Surface post-treatment with TMTA	Forward scan	1.12	24.8	76.6	21.3	0.018
	Reverse scan	1.14	24.8	76.6	21.7	
CSRC-treatment with TMTA	Forward scan	1.15	24.7	78.0	22.2	0.009
	Reverse scan	1.15	24.8	78.5	22.4	

Table S3. The fitted PL decay lifetimes of $FAPbI_3$ films with different TMTA treatment.

	Control device	CSRC-treatment with TMTA	Post-treatment with TMTA
A_1	8.14	48.9	17.046
τ_1 (ns)	112.4	180.8	151.3
A_2	115.1	440.5	57.3
τ_2 (ns)	1004.9	2796.1	1678.5
τ_{ave} (ns)	997.9	2777.5	1638.6